Phonon-limited carrier mobilities and Hall factors in 4*H*-SiC from first principles

Tianqi Deng [ORCID],[*] Deren Yang, and Xiaodong Pi [ORCID][†]

State Key Laboratory of Silicon and Advanced Semiconductor Materials & School of Materials Science and Engineering,
Zhejiang University, Hangzhou 310027, China
and Institute of Advanced Semiconductors & Zhejiang Provincial Key Laboratory of Power Semiconductor Materials and Devices,
ZJU-Hangzhou Global Scientific and Technological Innovation Center, Zhejiang University, Hangzhou 311215, China

Charge carrier mobility is at the core of semiconductor materials and devices optimization, and Hall measurement is one of the most important techniques for its characterization. The Hall factor, defined as the ratio between Hall and drift mobilities, is of particular importance. Here we study the effect of anisotropy by computing the drift and Hall mobility tensors of a technologically important wide-band-gap semiconductor, 4*H*-silicon carbide (4*H*-SiC), from first principles. With *GW* electronic structure and *ab initio* electron-phonon interactions, we solve the Boltzmann transport equation without fitting parameters. The calculated electron and hole mobilities agree with experimental data. The electron Hall factor strongly depends on the direction of external magnetic field **B**, and the hole Hall factor exhibits different temperature dependency for **B** ∥ *c* and **B** ⊥ *c*. We explain this by the different equienergy surface shape arising from the anisotropic and nonparabolic band structure, together with the energy-dependent electron-phonon scattering.

I. INTRODUCTION

Increasing demands in high-power and high-temperature electronic devices call for wide-band-gap semiconductors as the alternative functional materials to silicon. Silicon carbide (SiC) has become one of the most promising materials in power electronic devices owing to its unique combination of high carrier mobility, high critical field strength, high saturation velocity, and high thermal conductivity [1–6]. Among the more than 200 polytypes, 4*H*-SiC is preferred for its wider band gap and higher critical electric field than the cubic 3*C*-SiC and higher carrier mobilities and lower anisotropy as compared to 6*H*-SiC. Therefore, it is more technologically relevant and has become the major functional SiC polytype for applications in electronic devices [1].

Despite the recent surge of academic and industrial interests in 4*H*-SiC, many important aspects of its physical properties and the underlying physics are not clarified yet. For example, as a hexagonal crystal, anisotropy is expected for its physical properties like mechanical [7] and transport properties [1] such as carrier mobilities and the Hall effect. The carrier mobility is a key functional property that determines device performance such as on-resistance [8]. The Hall factor is needed to determine drift mobility from Hall measurement, and to clarify whether the Hall mobility anisotropy and temperature dependence mainly arises from the drift mobility contribution or from the Hall factor contribution. However, it is difficult to experimentally determine Hall factor directly. In practice, the Hall factors are commonly assumed to be $r_H = 1$, estimated using empirically parameterized models, or cal-

culated through carrier concentration estimated from dopant density and activation energies [8–13]. Additionally, the analysis of one of most important mechanisms underlying its charge transport phenomena, i.e., the electron-phonon interactions and scatterings, still relies on empirically determined, adjustable parameters with significant uncertainty. These adjustable parameters were also employed to explain exotic phenomena such as nonunity hole Hall factors [9,11,12,14]. Therefore, it becomes increasingly important to investigate such microscopic physics and confirm their respective contributions in the charge transport process without resorting to uncertain fitting parameters.

Electron-phonon interactions from the density functional perturbation theory (DFPT) calculations [15] emerged as a powerful tool for studying importance solid state phenomena and their underlying microscopic mechanisms, including phonon-limited charge transport [16–18], superconductivity [19,20], polaron [21,22], phonon-assisted optical absorption [23], band structure renormalization [24,25], etc. In conjunction with the Boltzmann transport equation (BTE), the charge transport in the presence of electrical field and magnetic field can be simulated self-consistently to obtain key quantities like drift mobility [16], breakdown field [26], and thermoelectricity [27]. Recently, the Hall effects in several typical cubic semiconductors have been studied by solving the BTE in the presence of both electric and magnetic fields, where quantitative agreement has been achieved in comparison with experimental measurements [18]. It is thus intriguing to explore the possible anisotropy in the hexagonal phase, to compute the Hall factors in the intrinsic limit, and to clarify the role of electron-phonon interactions in 4*H*-SiC.

In this work we perform an in-depth analysis of electron-phonon interactions, phonon-limited charge transport, and their anisotropy in 4*H*-SiC by first-principles calculations
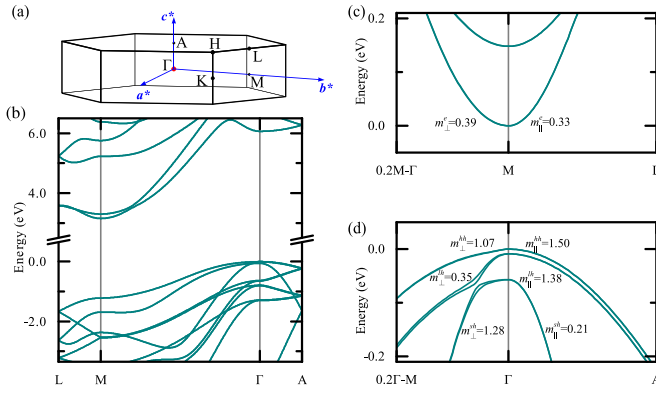
---

[*]dengtq@zju.edu.cn
[†]xdpi@zju.edu.cn

FIG. 1. (a) First Brillouin zone of 4*H*-SiC and band structure along high-symmetry path L-M-Γ-A. The band structure of (b) conduction and (c) valence bands near the band edges is also shown together with the effective masses along (∥) and perpendicular to (⊥) the *c* axis.

with accurate band structure shown in Fig. 1(a). Both short-ranged and long-ranged dipolar/quadrupolar electron-phonon interactions are included from first principles in combination with the Wannier-interpolation technique [18,28–31]. We find that the spin-orbit coupling (SOC) significantly affects the hole effective masses, even though the SOC splitting is small. The phonon-limited mobilities agree well with experimental measurements of lightly doped samples, and hole mobility exhibits a stronger anisotropy than that of electron. The electrons are mainly scattered by optical phonons, while the band-edge holes are mostly scattered by acoustic phonons at room temperature. The Hall factors depend on the directions of both the applied magnetic field and the electric current. Hall factors deviate from 1 for both electrons and holes, and distinct temperature dependence was predicted. The nonunity is explained by nonparabolic band structure, nonspherical equienergy surface, and energy-dependent electron-phonon scattering strength. This work thus clarifies the anisotropic charge transport phenomena in 4*H*-SiC and the impact of electron-phonon interactions in the intrinsic limit from a microscopic, *ab initio* perspective. The predicted Hall factors without empirical, adjustable parameters also allow possible comparison between drift mobility and Hall mobility from experimental measurements.

II. METHODS

A. Carrier mobility and Hall effect calculations

In a typical Hall measurement for Hall mobility along α direction, an electric current density **j** along α and magnetic field **B** along γ are applied, and the induced Hall field **E** and corresponding Hall voltage along β are measured, where α, β, and γ are orthogonal. In the linear regime of small B_γ, the Hall coefficient is

$$R^H_{\alpha\beta\gamma} = \frac{E_\beta}{j_\alpha B_\gamma} = \frac{[\sigma^{-1}(B_\gamma) - \sigma^{-1}(0)]_{\beta\alpha}}{B_\gamma}$$

$$\approx \left[\sigma^{-1}(0)\frac{\sigma(B_\gamma) - \sigma(0)}{B_\gamma}\sigma^{-1}(0)\right]_{\beta\alpha}. \quad (1)$$

Therefore, the calculation of the carrier mobility and Hall coefficient involves computing the magnetic field **B**-dependent conductivity tensor

$$[\sigma(\mathbf{B})]_{\alpha\beta} = \frac{-e}{V_{uc}}\sum_n\int_{\text{BZ}}\frac{d^3k}{\Omega_{\text{BZ}}}v_{n\mathbf{k}\alpha}\partial_{E_\beta}f^{\mathbf{B}}_{n\mathbf{k}}. \quad (2)$$

Here V_{uc} is the unit-cell volume, $v_{n\mathbf{k}\alpha} = \frac{\partial\varepsilon_{n\mathbf{k}}}{\partial\hbar k_\alpha}$ is the band velocity defined as the **k** derivative of eigenenergy $\varepsilon_{n\mathbf{k}}$ along α direction, and $\partial_{E_\beta}f^{\mathbf{B}}_{n\mathbf{k}}$ is the solution of the linearized BTE with magnetic field **B**:

$$-ev_{n\mathbf{k}\beta}\frac{\partial f^0_{n\mathbf{k}}}{\partial\varepsilon_{n\mathbf{k}}} - \frac{e}{\hbar}(\mathbf{v}_{n\mathbf{k}}\times\mathbf{B})\cdot\nabla_\mathbf{k}\partial_{E_\beta}f^{\mathbf{B}}_{n\mathbf{k}}$$

$$= \sum_m\int_{\text{BZ}}\frac{d^3q}{\Omega_{\text{BZ}}}\left(\tau^{-1}_{m\mathbf{k}+\mathbf{q}\rightarrow n\mathbf{k}}\partial_{E_\beta}f^{\mathbf{B}}_{m\mathbf{k}+\mathbf{q}} - \tau^{-1}_{n\mathbf{k}\rightarrow m\mathbf{k}+\mathbf{q}}\partial_{E_\beta}f^{\mathbf{B}}_{n\mathbf{k}}\right), \quad (3)$$

with $f^0_{n\mathbf{k}}$ and Ω_{BZ} being the equilibrium Fermi-Dirac distribution and first Brillouin zone volume, and electron-phonon (*e-ph*) scattering rate defined as

$$\tau^{-1}_{n\mathbf{k}\rightarrow m\mathbf{k}+\mathbf{q}} = \frac{2\pi}{\hbar}\sum_\nu|g_{mn\nu}(\mathbf{k},\mathbf{q})|^2$$

$$\times\left[(n_{\nu\mathbf{q}}+1-f^0_{m\mathbf{k}+\mathbf{q}})\delta(\varepsilon_{n\mathbf{k}}-\varepsilon_{m\mathbf{k}+\mathbf{q}}-\hbar\omega_{\nu\mathbf{q}})\right.$$

$$\left.+(n_{\nu\mathbf{q}}+f^0_{m\mathbf{k}+\mathbf{q}})\delta(\varepsilon_{n\mathbf{k}}-\varepsilon_{m\mathbf{k}+\mathbf{q}}+\hbar\omega_{\nu\mathbf{q}})\right]. \quad (4)$$

The *e-ph* matrix element $g_{mn\nu}(\mathbf{k},\mathbf{q})$ is induced by a phonon $\nu\mathbf{q}$ that scatters an electron from state $|n\mathbf{k}\rangle$ to $|m\mathbf{k}+\mathbf{q}\rangle$, and $n_{\nu\mathbf{q}}$ is the equilibrium Bose-Einstein distribution.

The BTE can be further recast into a form that is more suitable for iterative solution:

$$\left[1-\frac{e}{\hbar}\tau_{n\mathbf{k}}(\mathbf{v}_{n\mathbf{k}}\times\mathbf{B})\cdot\nabla_\mathbf{k}\right]\partial_{E_\beta}f^{\mathbf{B}}_{n\mathbf{k}}$$

$$= ev_{n\mathbf{k}\beta}\tau_{n\mathbf{k}}\frac{\partial f^0_{n\mathbf{k}}}{\partial\varepsilon_{n\mathbf{k}}} + \frac{2\pi\tau_{n\mathbf{k}}}{\hbar}$$

$$\times\sum_m\int_{\text{BZ}}\frac{d^3q}{\Omega_{\text{BZ}}}\left(\tau^{-1}_{m\mathbf{k}+\mathbf{q}\rightarrow n\mathbf{k}}\partial_{E_\beta}f^{\mathbf{B}}_{m\mathbf{k}+\mathbf{q}}\right). \quad (5)$$

The total scattering time is

$$\tau^{-1}_{n\mathbf{k}} = \sum_m\int_{\text{BZ}}\frac{d^3q}{\Omega_{\text{BZ}}}\tau^{-1}_{n\mathbf{k}\rightarrow m\mathbf{k}+\mathbf{q}}. \quad (6)$$

The above equations can be solved from first principles without any empirical parameters [17,18,32,33]. By solving Eq. (5) iteratively one obtains the self-consistent solution of $\partial_{E_\beta}f^{\mathbf{B}}_{n\mathbf{k}}$. One common approximated solution is the so-called self-energy relaxation time approximation (SERTA), which is computed using the scattering time $\tau_{n\mathbf{k}}$ by omitting the second term on the right-hand side of Eq. (5). This is equivalent to the first step in an iterative solution of Eq. (5). Further approximation, i.e., the constant relaxation time approximation (CRTA), can be made by assuming $\tau_{n\mathbf{k}}$ to be a universal constant τ_0 such that only band structure information is included.

Given the Hall coefficient and conductivity tensor, the Hall mobility along α direction with B_γ can be computed as

$$\mu^{\text{H},B_\gamma}_\alpha = \sigma_{\alpha\alpha}R_{\alpha\beta\gamma}, \quad (7)$$

and the drift mobility is

$$\mu_\alpha = \frac{\sigma_{\alpha\alpha}}{ne}. \tag{8}$$

Thus the Hall factor is the ratio between Hall and drift mobility

$$r_{\alpha\beta\gamma}^{\mathrm{H}} = \frac{\mu_\alpha^{\mathrm{H},B_\gamma}}{\mu_\alpha} = R_{\alpha\beta\gamma}ne. \tag{9}$$

B. First principles calculations

Evaluation of the *e-ph* scattering rate in Eq. (4) requires knowledge of $g_{mn\nu}(\mathbf{k},\mathbf{q})$ and $\varepsilon_{n\mathbf{k}}$ in the whole Brillouin zone. Here we compute the band structure $\varepsilon_{n\mathbf{k}}$ using density functional theory on a 8×8×2 **k** grid, which is sufficient for accurate Wannier-interpolation as shown in Appendix A. The $g_{mn\nu}(\mathbf{k},\mathbf{q})$ on the same **k**/**q** grid were calculated using relativistic DFPT [15] as implemented in QUANTUM ESPRESSO [34,35]. Subsequent Fourier-Wannier-interpolation onto much finer grids [36] using maximally localized Wannier functions [37,38] were carried out with EPW software [39,40]. Dipolar and quadrupolar corrections to the interpolation were also included [18,28–31,41–43], with Born effective charge $\mathbf{Z}_\kappa^*$, dielectric ε_∞, and dynamical quadrupole tensors $\mathbf{Q}_\kappa^*$ calculated from linear response [44,45] as implemented in QUANTUM ESPRESSO [34,35] and ABINIT [46,47]. The *e-ph* matrix element $g_{mn\nu}(\mathbf{k},\mathbf{q})$ contains the long-ranged part arising from dipolar

$$g_{mn\nu}^{L,D}(\mathbf{k},\mathbf{q}) = i\frac{4\pi}{V_{uc}}\frac{e^2}{4\pi\varepsilon_0}\sum_\kappa\left(\frac{\hbar}{2N_pM_\kappa\omega_{\nu\mathbf{q}}}\right)^{1/2}$$
$$\times\sum_{\mathbf{G}\neq\mathbf{q}}\frac{(\mathbf{G}+\mathbf{q})\cdot\mathbf{Z}_\kappa^*\cdot\mathbf{e}_{\kappa\nu\mathbf{q}}e^{-i(\mathbf{G}+\mathbf{q})\cdot\tau_\kappa}}{(\mathbf{G}+\mathbf{q})\cdot\varepsilon_\infty\cdot(\mathbf{G}+\mathbf{q})}(U_{\mathbf{k}+\mathbf{q}}U_\mathbf{k}^\dagger)_{mn} \tag{10}$$

and quadrupolar interactions

$$g_{mn\nu}^{L,Q}(\mathbf{k},\mathbf{q}) = \frac{4\pi}{V_{uc}}\frac{e^2}{4\pi\varepsilon_0}\sum_\kappa\left(\frac{\hbar}{2N_pM_\kappa\omega_{\nu\mathbf{q}}}\right)^{1/2}$$
$$\times\sum_{\mathbf{G}\neq\mathbf{q}}\frac{(\mathbf{G}+\mathbf{q})\cdot(\mathbf{G}+\mathbf{q})\cdot\mathbf{Q}_\kappa^*\cdot\mathbf{e}_{\kappa\nu\mathbf{q}}e^{-i(\mathbf{G}+\mathbf{q})\cdot\tau_\kappa}}{2(\mathbf{G}+\mathbf{q})\cdot\varepsilon_\infty\cdot(\mathbf{G}+\mathbf{q})}$$
$$\times(U_{\mathbf{k}+\mathbf{q}}U_\mathbf{k}^\dagger)_{mn}, \tag{11}$$

where the Z_κ^* contribution to the quadrupolar interactions were neglected [18]. Here $e_{\kappa\nu q}$ is the eigendisplacement of atom κ in phonon mode νq, and $U_\mathbf{k}$ is the Wannier rotation matrix.

PBEsol generalized gradient approximation [48] and norm-conserving pseudopotentials from PseudoDojo project [49] with a wave-function cutoff energy of 90 Ry were used for the structural relaxation and DFPT calculations. The relaxed lattice constants are $a = 3.0787$ Å and $c = 10.0785$ Å, and they agree well with the experimentally measured room temperature values of $a = 3.0798$ Å and $c = 10.0820$ Å, considering the small thermal expansion coefficients of $\alpha_{11} \approx 3.21\times10^{-6}$ and $\alpha_{33} \approx 3.09\times10^{-6}$ [1]. The *GW* quasiparticle band structure $\varepsilon_{n\mathbf{k}}$ is computed using YAMBO [50,51] at the G_0W_0 level with plasmon-pole approximation for the screening. Here 800 bands were used for the screening and

TABLE I. The effective masses of electrons (*e*) and holes (*hh* for heavy hole, *lh* for light hole, and *sh* for crystal-field split-off hole) along transverse (⊥, in basal plane) and longitudinal (∥, along the *c* axis) directions. All masses are given in the unit of electron rest mass m_e.

		Without SOC		With SOC		
		HSE	*GW*	HSE	*GW*	Exp.
$m_\perp^e$	$m_{\mathrm{M}\Gamma}^e$	0.58	0.54	0.58	0.54	0.58 ± 0.01 [54]
	m_{MK}^e	0.28	0.29	0.28	0.29	0.31 ± 0.01 [54]
	$m_\perp^e$	0.4	0.39	0.4	0.39	0.425 [54]
$m_\parallel^e$	$m_\parallel^e$	0.34	0.33	0.34	0.33	0.33 ± 0.01 [54]
$m_\perp^h$	$m_\perp^{hh}$	3.04	12.9	0.64	0.65	0.66 ± 0.02 [55]
	$m_\perp^{lh}$	0.29	0.31	0.45	0.44	
	$m_\perp^{sh}$	1.37	1.14	1.40	1.42	
$m_\parallel^h$	$m_\parallel^{hh}$	1.48	1.48	1.48	1.50	1.75 ± 0.02 [55]
	$m_\parallel^{lh}$	1.48	1.48	1.30	1.35	
	$m_\parallel^{sh}$	0.20	0.20	0.20	0.21	

Green's function calculations, and the exchange and dielectric function cutoff energies were 360 Ry and 40 Ry, respectively. Hybrid functional band structure was computed with HSE06 functional [52,53] using the same 90 Ry cutoff and 8×8×2 **k** grid for both the wave functions and the exchange (Fock) operator.

III. RESULTS AND DISCUSSION

A. Band structure

We first compare the computed effective masses with those from experiments [54,55], as detailed in Table I. The effective masses are computed through polynomial fitting of the band structure near band extrema, as shown in Fig. 1. Since the valence bands are very anisotropic and nonparabolic, quartic polynomials were used for them, and the effective masses were computed from the quadratic term coefficients. The conduction band edge is at M point, as shown in Figs. 1(a) and 1(b), and the valley is anisotropic in all three directions. The electron effective mass is almost not affected by band structure method (*GW* and HSE) or spin-orbit coupling (SOC), possibly due to the low intravalley degeneracy. The transverse electron effective mass $m_\perp^e$ in the basal plane, which is the average of effective masses along M-K and M-Γ directions, is around 0.39. The longitudinal electron effective mass $m_\parallel^e$ along the *c* axis (M-L direction) is calculated to be around 0.33. All components of electron effective masses are very close to the experimental values from cyclotron resonance measurements [54]. On the other hand, the hole effective mass is strongly affected by the SOC, while *GW* shows very small improvement over HSE. The measured transverse hole effective mass $m_\perp^e$ of 0.66 ± 0.02 is very close to the predicted heavy hole (*hh*) effective mass from *GW*+SOC calculation [55]. The measured longitudinal hole effective mass $m_\parallel^e$ of 1.75 ± 0.02 is 17% heavier than the predicted value. Considering the low measurement temperature (4 K) and large SOC gap between *hh* and *lh* bands (10 meV), only *hh* near VBM should be occupied and contributing to the cyclotron resonance signals, as discussed in Ref. [55]. Overall, the
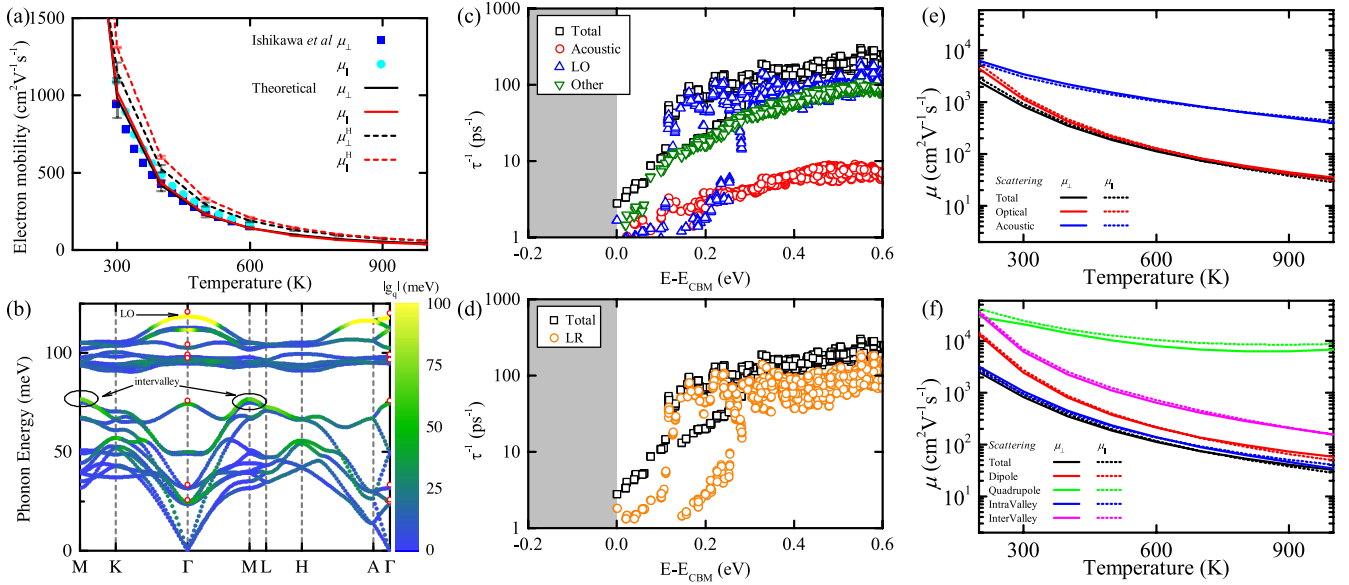
FIG. 2. (a) Anisotropic electron mobilities compared with experimentally measured values by Ishikawa *et al.* [13]. (b) The mode-resolved electron-phonon interactions $|g_{mn\nu}(\mathbf{k}, \mathbf{q})|$ with the initial state $m\mathbf{k}$ at conduction band edge (M point) and $\mathbf{q}$ along a high-symmetry path. The red circles mark the phonon energy measured at $10\,°C$ [57]. Contributions of acoustic phonons, longitudinal optical (LO) phonons, and other optical phonons are compared with the total electron scattering rate at 300 K in (c). The long-ranged (LR) *e-ph* interactions contributions are shown in (d). On top of the scattering rate analysis, the mobility limited by (e) acoustic and optical phonon branches and (f) certain scattering mechanisms including dipolar, quadrupolar, intravalley, and intervalley scatterings are also compared with the mobility calculated with all mechanisms included.

electron effective mass predictions are closer to the experimental counterparts than those for holes, similar to the case of Si [56].

B. Intrinsic mobility

By solving the full-band BTE iteratively, we compute carrier mobilities using Eq. (1) to (8). The GW+SOC band structure and electron-phonon matrix elements from PBEsol calculations were employed in the BTE. An adaptively broadened Gaussian function was employed to approximate the energy-conserving Dirac function [18]. By increasing the density of $\mathbf{k}/\mathbf{q}$ Brillouin zone mesh sampling from $15\times15\times5$ to $75\times75\times25$, we observe a rapid convergence of the drift mobilities. The Hall mobility, on the other hand, converges slower with a linear trend in $\mathbf{k}$-mesh density $1/N_k$ towards $N_k \to \infty$. Therefore, we linearly extrapolate the mobility data towards $N_k \to \infty$ following Poncé *et al.* [18] using the three points with densest $\mathbf{k}$ mesh, as detailed in Appendix B. Error bars from least-squared fitting are also shown in Figs. 2(a), 3(a), and 4.

We first compare the computed anisotropic electron mobilities with experimental measurement on an epitaxial sample fabricated on SiC $(11\bar{2}0)$ substrate with a donor density of $2.1\times10^{15}\mathrm{cm}^{-3}$ [13]. As shown in Fig. 2(a), the experimentally measured Hall mobilities are slightly lower than the predicted phonon-limited Hall mobilities and close to the predicted drift mobilities. This is expected as additional scattering mechanisms such as impurities are not included in the calculations. The temperature dependence is also studied by fitting with a power-law relation, $\mu \propto T^{-\beta}$. The typical β value for lightly

n-doped 4H-SiC is 2.4 to 2.8 [1], while Ishikawa *et al.* [13] found an decreasing β with increased doping concentration with highest $\beta = 2.67$ for $\mu_{\parallel}^{H}$ and $\beta = 2.58$ for $\mu_{\perp}^{H}$ at donor concentration of $2.1\times10^{15}\mathrm{cm}^{-3}$. The calculated β in this work is 2.82 ± 0.03 for $\mu_{\parallel}^{H}$ and 2.83 ± 0.03 for $\mu_{\perp}^{H}$, which is expected to be the intrinsic limit. The stronger T dependence of intrinsic mobility is expected as defect scatterings are absent and the strongly T-dependent *e-ph* scattering is the only mobility-limiting factor.

Next we investigate the mode-resolved contributions to the *e-ph* scatterings. As shown in Fig. 2(c), most of the scatterings for high-energy electrons are contributed by the optical phonons, particularly the polar longitudinal optical (LO) phonons. Near the conduction band edge, the LO phonon contribution reduces due to energy mismatch, and the low-energy electrons are scattered by all phonon branches. Moreover, by computing the scattering rate only with long-ranged (LR) interactions, i.e., those from dipolar and quadrupolar *e-ph* interactions in Eq. (10) and Eq. (11), LR contribution is revealed to be important for both high- and low-energy electrons as shown in Fig. 2(d). The dominance of optical phonon scatterings can also be observed in Fig. 2(e) where the optical-phonon limited mobility is very close to the final mobility with all scatterings. The importance of acoustic phonons is comparable only to optical phonons at lower temperature where the optical phonon populations are significantly reduced. For example, at 200 K, the acoustic-phonon-limited mobility is very close to the optical-phonon-limited one. At 300 K, however, the acoustic-phonon-limited mobility is about three times that of optical phonons. Further decomposition into scattering mechanisms in Fig. 2(f) shows that the dipolar part
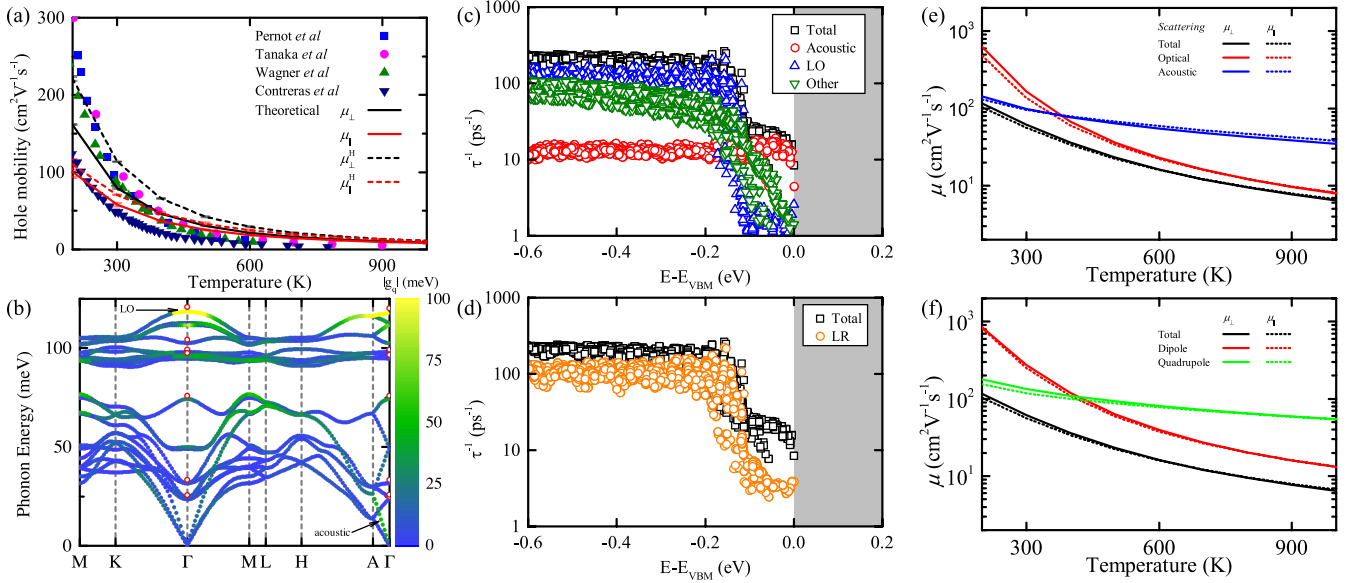
FIG. 3. (a) Anisotropic hole mobilities compared with experimental measurement from the literature [12,60–62]. (b) Mode-resolved electron-phonon interactions $|g_{mnv}(\mathbf{k}, \mathbf{q})|$ with heavy hole state at valence band edge (Γ point) being initial state $m\mathbf{k}$ and $\mathbf{q}$ along the high-symmetry path. The red circles mark the phonon energy measured at 10 °C [57]. Contributions of acoustic phonons, longitudinal optical (LO) phonons, and other optical phonons are compared with the total hole scattering rate at 300 K in (c). The long-ranged (LR) e-ph interactions contributions are shown in (d).
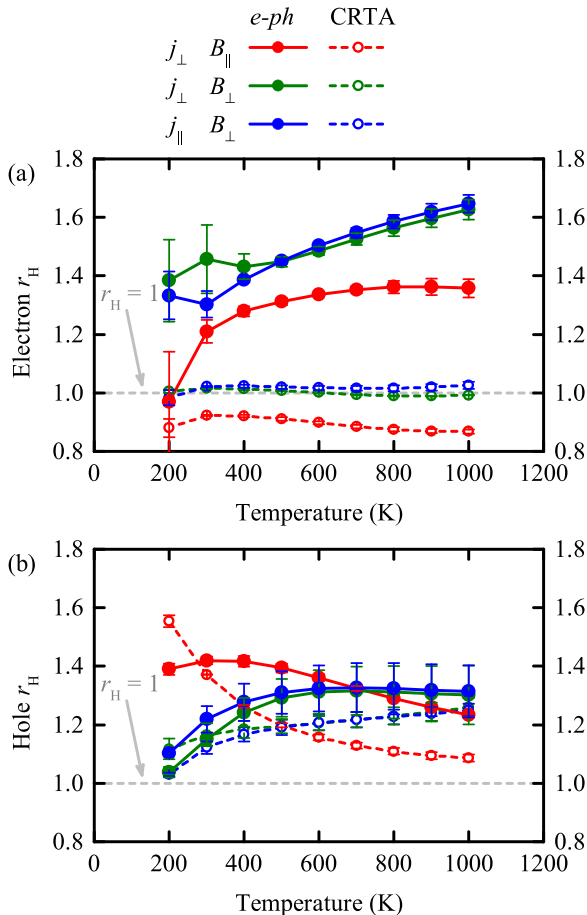

FIG. 4. Hall factor r_H for (a) electrons and (b) holes for current j and magnetic field $\mathbf{B}$ parallel to ($\parallel$) or perpendicular to ($\perp$) the c axis.

of long-ranged e-ph scatterings dominate over the quadrupolar contribution, in line with the observation that the LO phonon couples most strongly with electrons shown in Fig. 2(b). In the case of GaN, a similar hexagonal semiconductor with piezoelectricity, inclusion of quadrupolar effect was demonstrated to be critical for correctly predicting e-ph interactions, while the e-LO coupling is also the dominant scattering channel for electrons [31]. The intervalley scattering is much weaker than the long-wavelength intravalley scattering. It can be seen from Fig. 2(d) that even for high-energy electrons, the long-ranged interactions are still the dominant scattering mechanism, in contrast to the case of GaAs [42]. This is because the second electron valley in 4*H*-SiC is at least 2 eV higher as shown in Fig. 1(a), unlike the case of GaAs, which was only 0.3 eV.

For further clarification of scattering mechanisms, the e-ph interactions between the conduction band edge state at the M point and phonons along the high-symmetry path are visualized in Fig. 2(b). It is evident that the electron-LO-phonon interactions are the strongest due to the diverging Fröhlich interaction from nonzero Born effective charges whose average values are $\overline{Z^*_\parallel} \approx 2.78$ and $\overline{Z^*_\perp} \approx 2.68$, respectively. The full Born effective charge and dynamical quadrupole tensors are tabulated and discussed in Appendix C. Additionally, the optical phonons around 75 meV at M point, which could scatter the electrons at one M valley to another M valley, are also significant and become another major scattering mechanism apart from the Fröhlich interaction. e-ph interactions with other intervalley phonons branches are much weaker. The interactions with acoustic phonons are rather weak, which could be attributed to the *floating* nature of conducting electrons in SiC, whose wave functions are away from atoms or bonds [58]. The short-ranged part of electron-ion interactions can be reduced in this case, resulting in weaker deformation potential. The deformation potential constants for electrons

are obtained from the slope of g, as tabulated in Table II in Appendix C. Indeed, the average value of 3.76 eV is weaker than that of holes, 7.10 eV, and that of electrons in silicon, 8.21 eV [59].

The hole mobilities are also computed and compared with experimental values from several references [12,60–62], as shown in Fig. 3(a). The experimental data were all measured for epilayers on (0001) or slightly off-axis (0001) substrate. Therefore, the measured mobility should be close to the in-basal-plane component and are compared with $\mu_\perp$. While the measured mobilities are close to or lower than the computed Hall mobility $\mu_\perp^H$ around room temperature, at higher temperature the measured mobility decreases at a faster rate than the predictions. Previous studies attributed the strong decrease partially to the reduced hole Hall factor at high temperature, which can be further reduced by high doping levels [11,12]. The impact of e-ph interactions on Hall factor will be further discussed in the next section.

The hole scattering rates are also decomposed into different phonon branches, as shown in Figs. 3(c) to 3(e). The holes at valence band edge are mainly scattered by acoustic phonons, while at higher energy above 0.1 eV the optical phonon scatterings are dominant since the emission of high-frequency optical phonons becomes available in this region. This, in conjunction with the enhanced optical phonon population at high temperature, explains the change of dominant scatterers from acoustic phonons below 400 K to optical phonons above 400 K, as shown in Fig. 3(e). At 300 K, the acoustic phonon is the dominant scatterer for band edge holes as shown in Figs. 3(c) and 3(e). The acoustic phonon contribution to the scattering rates exhibits very weak energy dependence, as shown in Fig. 3(c). This can be explained by the counterbalance between the $\tau^{-1} \propto E^{1/2}$ trend of the deformation potential scattering and the $\tau^{-1} \propto E^{-1/2}$ trend of the piezoelectric scattering [63], similar to the observations in GaAs [64] and GaN [31]. The strong deformation potential (7.10 eV on average) scattering arises from the sp^3 bond nature of the valence states (holes), which can strongly couple with the atomic displacement through bond distortion. Although the intermediate-frequency intervalley phonons still couple strongly with holes, there is no final states available for scattering as the valence band edge is centered at the Γ point. Therefore, the holes are mainly scattered by intravalley acoustic and optical phonons.

C. Hall factor

Using the fully *ab initio* band structure without resorting to approximate parabolic or $k \cdot p$ band models, we first compute the Hall factor tensors in the constant relaxation time approximation without considering the scattering mechanisms. In this case, we eliminate the impact of scattering, and their deviation from $r_H = 1$ solely reflects the realistic band structure, i.e., the band multiplicity, anisotropy, and nonparabolicity.

As shown in Fig. 4(a), the electron Hall factors are not significantly temperature dependent. When the magnetic field $\mathbf{B}_\parallel$ is applied along the c axis, r_H is around 0.9. The deviation from 1 is attributed to the in-plane anisotropy of the conduction valley, where the electron effective mass along M-Γ direction is about twice that of M-K direction, leading
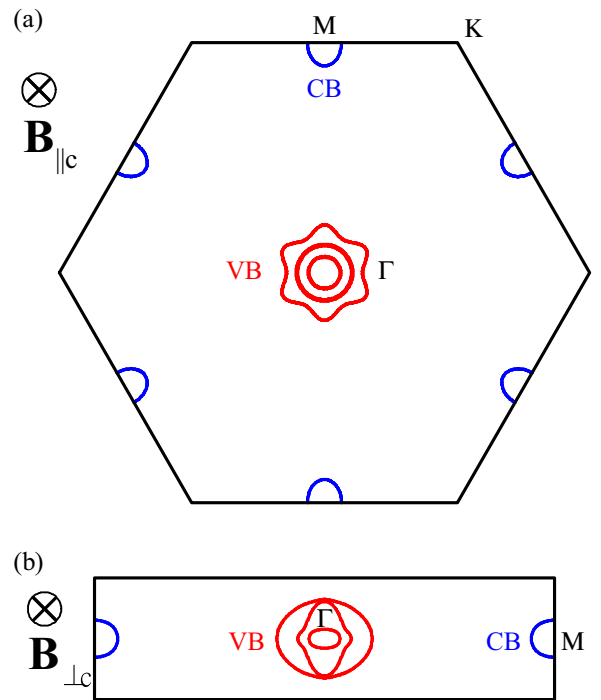

FIG. 5. Equienergy lines of conduction (blue) and valence (red) bands in a $\mathbf{k}$-plane perpendicular to the applied magnetic field, with (a) $\mathbf{B}$ along the c axis and (b) $\mathbf{B}$ perpendicular to the c axis, respectively. The equienergy lines are 0.1 eV above the conduction band edge and below the valence band edge.

to the elliptic equienergy line shown in Fig. 5(a). When $\mathbf{B}_\perp$ is applied, the mass anisotropy in the planes perpendicular to $\mathbf{B}_\perp$ is reduced because $m_\parallel^e$ is between $m_{\mathrm{M}\Gamma}^e$ and $m_{\mathrm{M}\Gamma}^e$. Therefore, the Hall factors with $\mathbf{B}_\perp$ are very close to 1 as shown in Fig. 4(a).

The case of holes is more complicated. The *hh* and *lh* bands are energetically close and are all involved in the transport process at the temperatures studied here. Moreover, these bands are very anisotropic and nonparabolic in the vicinity of the valence band edge, as revealed by the effective masses and equienergy line shape (Fig. 5). Therefore, a deviation from unity is naturally expected even without any specific scattering mechanism as in CRTA. Indeed, the computed hole Hall factors are all away from unity. Interestingly, we observed different temperature-dependent Hall factors when magnetic fields are applied in different directions: when $B_\parallel$ is applied, r_H decreases as temperature increases; when $B_\perp$ is applied, r_H slightly increases at higher temperature. Such behaviors can be traced back to the equienergy line shapes of different bands. As illustrated in Fig. 5, in the (0001) plane, the low-energy heavy-hole *hh* bands shows a complex, nonelliptic equienergy line, while the high-energy *lh* bands have an almost isotropic, circular equienergy line. Therefore, as temperature increases, *lh* bands participate in the transport process, which explains the r_H approaching 1 at high temperature with $B_\parallel$. In the case of $B_\perp$, as shown in Fig. 5(b), the *hh* bands are elliptic while the *lh* band becomes nonelliptic. Therefore, r_H deviates further from 1 as the temperature increases.

When the e-ph interactions are included and the BTE is self-consistently solved, the Hall factor r_H changes drastically.

The electron r_H increases to as high as 1.6 at 1000 K and remains anisotropic depending on the direction of the applied magnetic field. Specifically, when the magnetic field is applied perpendicular to the c axis, the Hall factor is almost isotropic. But the value changes significantly when the magnetic field is switched to $B \parallel c$ axis, from around 1.6 to around 1.4 at high temperature. Additionally, the electron r_H is increasing with temperature in contrast to the CRTA results, which are almost constant across the studied temperature range. Similarly, the hole Hall factor is also different from CRTA results, but the change is less significant. This is attributed to the energy-dependent τ, whose contribution can be approximately described in isotropic case by the Hall scattering factor $r_s = \frac{\langle\langle \tau^2 \rangle\rangle}{\langle\langle \tau \rangle\rangle^2}$ where $\langle\langle \tau^i \rangle\rangle = \sum_{nk} \varepsilon_{nk} f_{nk} \tau^i_{nk} / \sum_{nk} \varepsilon_{nk} f_{nk}$ [63]. The computed r_s is 1.22 for electrons and 1.09 for holes at 300 K, which also reflects the different distributions of τ for electrons and holes near the band edge. The difference arises from both the difference in major scattering mechanisms, as discussed in the previous section, and the difference in band structure complexity. Due to the strong anisotropy, nonparabolicity, and band multiplicity, the available scattering phase space is more complex than the simple parabolic conduction band. This leads to not only the difference in CRTA r_H, but also different r_s in the presence of e-ph interactions.

The complexity in Hall factor temperature dependence has also been observed in many cubic semiconductors [18]. Poncé *et al.* found that Hall factors calculated from Boltzmann transport equations in magnetic field can be very different from those estimated through the isotropic model $r_s = \frac{\langle\langle \tau^2 \rangle\rangle}{\langle\langle \tau \rangle\rangle^2}$. The electrons in 4$H$-SiC studied in this work exhibit increasing Hall factors at elevated temperature, similar to the observations in Si, 3C-SiC, and c-BN. Some other n-type semiconductors may exhibit decreasing or more complicated temperature dependence. The rise-and-fall trend of hole Hall factors with $j_\perp$ and $B_\parallel$ is similar to those of GaAs and AlAs, while certain p-type semiconductors such as Si and AlP may exhibit a significant drop in hole r_H. Such complexity in simple semiconductors calls for further careful study of Hall effects to achieve solid and deep understanding of magneto-transport phenomena in different semiconductors.

We note that in previous references, the Hall factors (deduced from experimental Hall measurement, donor/acceptor density, and ionization energy) are lower than the BTE-predicted values in this work. Considering the agreement between theoretical and experimental effective masses, the discrepancy likely arises from the factors other than the band structure, including but not limited to scattering. For example, Asada *et al.* [11] revealed experimentally that the Hall factors showed a significant reduction with increased Al doping in 4H-SiC, suggesting that doping can be a factor that lowers the Hall factor. Tanaka *et al.* [12] computed the p-type 4H-SiC Hall factor and mobility using BTE in relaxation time approximation with a simplified phonon and impurity scattering model in conjunction with adjustable parameters. They assumed that the nonpolar optical phonon scattering may lead to a highly anisotropic scattering rate in the Basal plane direction ($\perp$) and reduces the Hall factor. However, by computing the phonon mode-resolved contributions to the
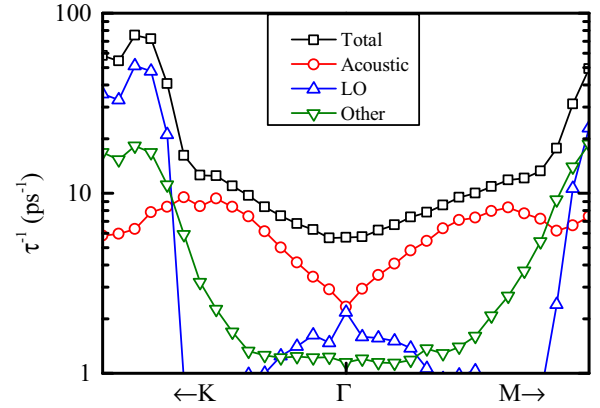

FIG. 6. Mode-resolved scattering rate of holes in a heavy hole band near the valence band edge. No significant anisotropy is observed for either the total scattering rate or contributions from individual phonon modes to the band edge holes.

total scattering rate, as shown in Fig. 6, it can be seen that both the total and mode-resolved scattering rates are almost isotropic in the basal plane. Therefore, the experimentally observed small Hall factors may not be explained by anisotropic phonon-limited scattering rate. Deeper understanding of such phenomena requires further in-depth study of these mechanisms, and the origin of the small Hall factor observed in doped 4H-SiC still remains an open question. Alternative explanations could be impurity scatterings, dislocation scatterings, and uncertainty in the estimated carrier concentrations in experimental works using a hydrogenic model, among others.

IV. CONCLUSIONS

In summary, we studied the phonon-limited electron and hole transport behaviors of 4H silicon carbide by solving the Boltzmann transport equation in conjunction with Wannier interpolation of band structure and electron-phonon interactions from density functional (perturbation) theory calculations. The resulting effective masses and carrier mobilities agree well with experimental measurement. The anisotropy of band structure, electron-phonon scattering, and carrier mobilities is investigated in detail. Spin-orbit interactions must be included
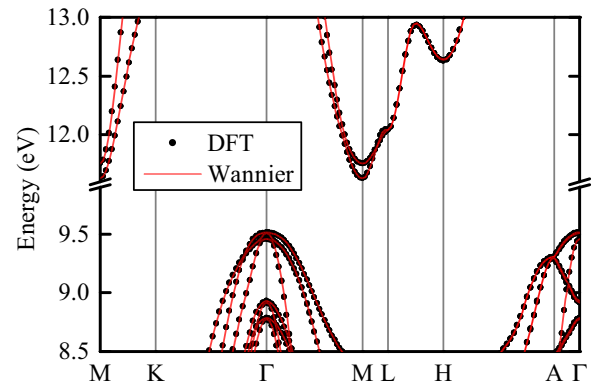

FIG. 7. Comparison between band structures computed using direct DFT calculation and using Wannier interpolation starting from a 8×8×2 **k**-mesh.
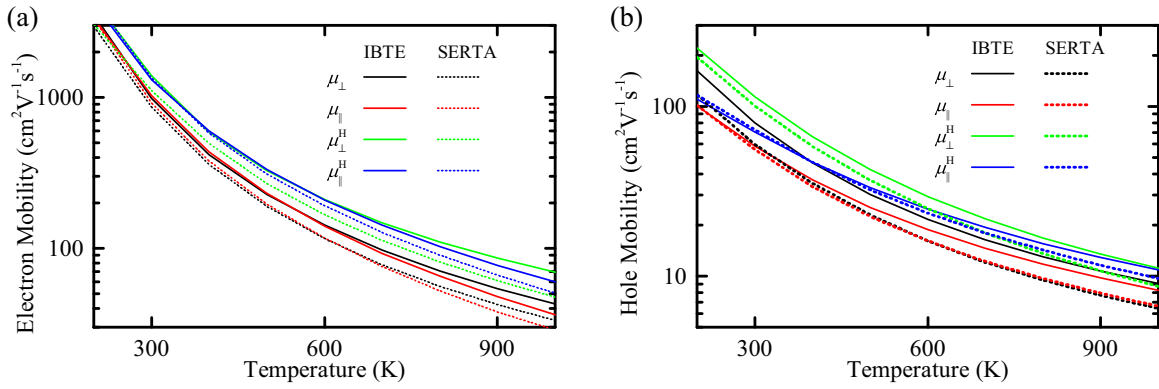
FIG. 8. Comparison between drift mobilities ($\mu_\parallel$, $\mu_\perp$) and Hall mobilities ($\mu_\parallel^H$, $\mu_\perp^H$) calculated using IBTE (solid lines) and SERTA (dotted lines).

to correctly reproduce the experimental valence band structure, while both HSE and *GW* calculations could excellently reproduce the experimental effective masses. We showed that the anisotropy of electron effective masses and mobilities is weaker than that of the holes, while both the electron and hole Hall factors are strongly direction and temperature dependent. The Hall factors significantly deviate from 1, which is explained by the energy-dependent electron-phonon scattering rate and anisotropic band structure. The results clarified the role of electron-phonon interactions in the transport phenomena of the technologically relevant 4*H*-SiC.

APPENDIX A: WANNIER INTERPOLATION OF BAND STRUCTURE

To test the Wannier interpolation reliability, we computed the band structure along a high-symmetry path using both direct DFT calculation and Wannier interpolation from a $8\times8\times2$ coarse **k** mesh, as shown in Fig. 7. The agreement is excellent for both conduction and valence bands.
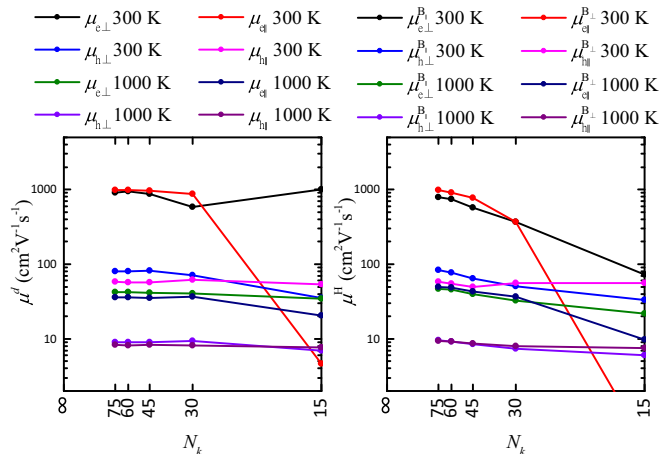

FIG. 9. Convergence of drift mobility μ and Hall mobility μ^H with respect to Brillouin zone sampling point number along one axis N_k. The same grid was used for both electron **k** and phonon **q**.
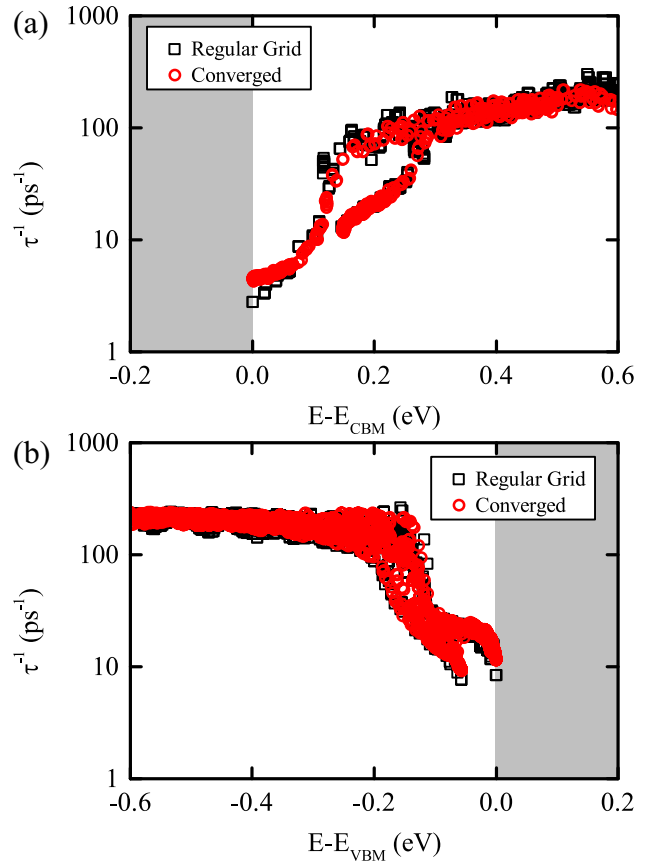
FIG. 10. (a) Electron and (b) hole scattering rates calculated using a $75\times75\times25$ regular Brillouin zone grid (black boxes), compared with those converged using Cauchy-Lorentz importance sampling (red circles).
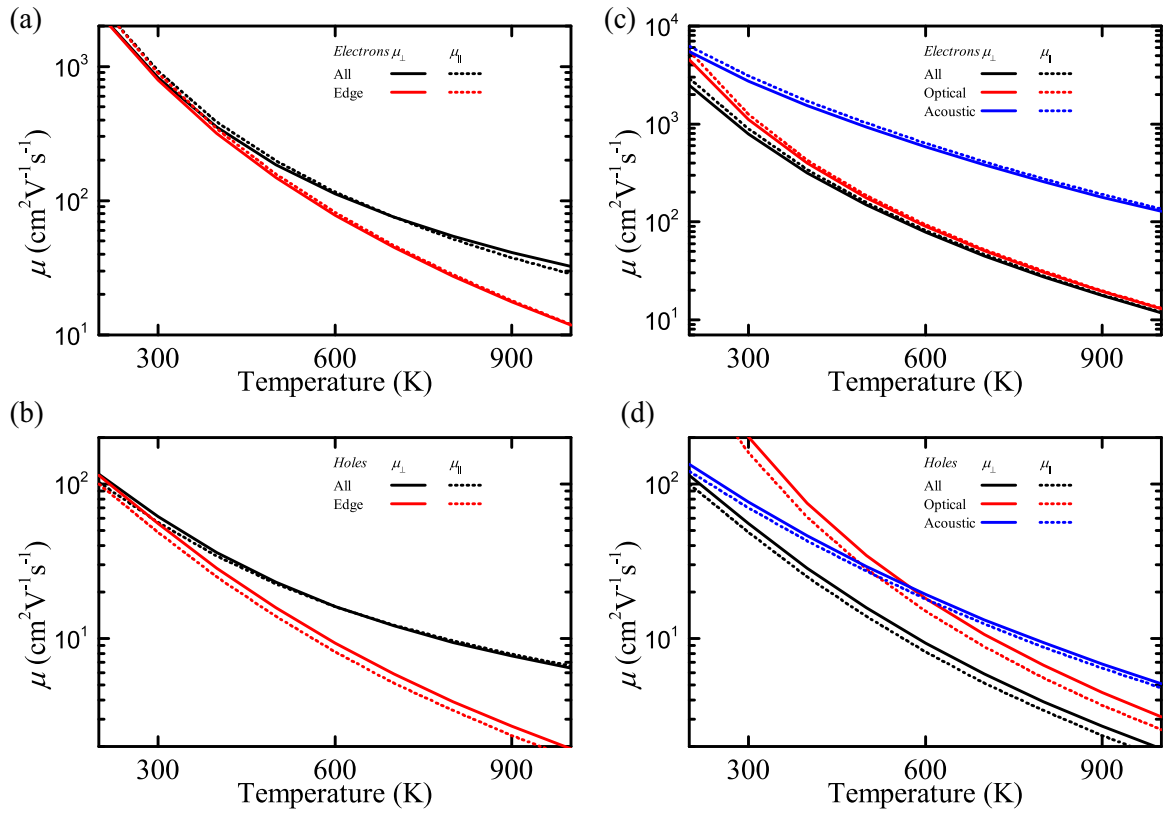
FIG. 11. (a) Electron and (b) hole mobilities with all charge carriers (black) and band-edge carriers only (red). The phonon-mode-decomposed mobilities for band-edge (c) electrons and (d) holes are also shown.

Therefore, the same Brillouin zone sampling is consistently used throughout this work. The Wannier functions are p-like orbitals centered on all C atoms for valence bands, and sp^3-like orbitals centered on all Si atoms for conduction bands, respectively.

APPENDIX B: IMPACT OF NUMERICAL CALCULATIONS ON THE MOBILITIES

The solution of BTE can be performed either self-consistently through iterations (IBTE) or by employing the so-called self-energy relaxation time approximation (SERTA). The drift and Hall mobilities using these two methods are compared in Fig. 8. In general, SERTA tends to underestimate both the drift and Hall mobilities, similar to the observation in cubic semiconductors [18,65].

Ideally, the mobility from BTE could converge to a constant value as the Brillouin zone sampling becomes infinitely dense. However, this is computationally unattainable. Therefore, a finite Brillouin zone sampling grid must be used, and its convergence should be tested. Since only a regular grid can be employed for an iterative BTE solution implemented in EPW, its convergence may not be as fast as importance sampling such as the Cauchy-Lorentz distribution [43,56]. As shown by Poncé *et al.* [18], in many cubic semiconductors both the drift and Hall mobility approach the converged value linearly in $1/N_k$ with N_k being the fine $\mathbf{k}/\mathbf{q}$ sample size along one direction. Here we also observed similar phenomena in the hexagonal 4H-SiC. As shown in Fig. 9, both the drift mobility

μ^d and Hall mobility μ^H steadily approach their respective converged values. Therefore, we used the densest three sampling grids for the linear extrapolation towards $N_k \to \infty$. Additionally, we compared the scattering rate from regular grid calculations with those using additional Cauchy-Lorentz samplings near electron band edge and phonon zone center, as shown in Fig. 10. While those calculated using regular grid for BTE shows some fluctuations, the convergence of mobilities and Hall factors can be well extrapolated, similar to the case of cubic semiconductors observed by Poncé *et al.* [18].

Both low-energy (band-edge) carriers and high-energy carriers participate into the charge transport. To understand their respective roles and characteristics, we compared the mobility from band-edge carriers within 0.1 eV above CBM (below VBM) with the overall mobility, as shown in Fig. 11. The discrepancy between overall and band-edge mobilities above 400 K indicates that high-energy carriers are dominant at high temperature. The phonon-mode-decomposed mobilities show similar trends as the overall mobilities in Figs. 2 and 3, but the optical phonons dominate only the hole scattering at higher temperature above 600 K, indicating relatively weaker optical phonon scattering at the band edge as compared to those for high-energy holes.

APPENDIX C: DIELECTRIC TENSOR, BORN EFFECTIVE CHARGES, AND DYNAMICAL QUADRUPOLE TENSORS

The space group of 4H-SiC is $P6_3mc$ (or C_{6v}^4 using the Schoenflies symbol) [1]. The Si and C atoms at the cubic

TABLE II. Components of dielectric tensor $\boldsymbol{\varepsilon}^\infty$, deformation potential D_{LA} for LA phonon, Born effective charges $\mathbf{Z}^*$, and dynamical quadrupole tensors $\tilde{\mathbf{Q}}$. Values from the literature are included for comparison.

		This work				Exp.
$\boldsymbol{\varepsilon}^\infty$	ε_{11}^∞	7.17				6.52 (6H [68])
	ε_{33}^∞	7.40				6.70 (6H [68])
D_{LA} (eV)	$D_{\Gamma K}^e$	5.10				
	$D_{\Gamma M}^e$	3.18				
	$D_{\Gamma A}^e$	2.51				
	$D_{\Gamma K}^h$	3.06				
	$D_{\Gamma M}^h$	3.68				
	$D_{\Gamma A}^h$	11.32				
		Si		C		
		k	h	k	h	
$\mathbf{Z}^*$	Z_{11}	2.69	2.68	−2.67	−2.71	$|\bar{Z}| = 2.70$ (6H [69])
	Z_{33}	2.92	2.64	−2.82	−2.74	
$\tilde{\mathbf{Q}}$	Q_{15}	3.44	3.88	−1.28	−1.08	
	Q_{22}	5.51	−5.04	−1.82	0.17	$Q_{Si} = 6.87$
	Q_{31}	3.33	4.02	−1.19	−0.88	$Q_C = −2.44$
	Q_{33}	−7.39	−7.63	3.47	2.84	(3C [18])

(k) sites occupy the $2a$ Wyckoff positions, while those at the hexagonal sites occupy the $2b$ Wyckoff positions. Both $2a$ and $2b$ sites have the trigonal $3m$ (C_{3v}) point group. Being rank-2 (rank-3) tensors, the Born effective charges (dynamical quadrupole tensors) share the same tensor shape and symmetry with the dielectric tensors (piezoelectric tensors) in the respective point group [66,67] where

$$\boldsymbol{\varepsilon}^\infty = \begin{pmatrix} \varepsilon_{11}^\infty & 0 & 0 \\ 0 & \varepsilon_{11}^\infty & 0 \\ 0 & 0 & \varepsilon_{33}^\infty \end{pmatrix}, \tag{C1}$$

$$\mathbf{Z}^* = \begin{pmatrix} Z_{11} & 0 & 0 \\ 0 & Z_{11} & 0 \\ 0 & 0 & Z_{33} \end{pmatrix}, \tag{C2}$$

$$\tilde{\mathbf{Q}} = \begin{pmatrix} 0 & 0 & 0 & 0 & Q_{15} & -Q_{22} \\ -Q_{22} & Q_{22} & 0 & Q_{15} & 0 & 0 \\ Q_{31} & Q_{31} & Q_{33} & 0 & 0 & 0 \end{pmatrix}. \tag{C3}$$

In the $\boldsymbol{\varepsilon}^\infty$ and $\mathbf{Z}^*$ tensor, $\{1, 2, 3\}$ refers to the Cartesian directions $\{x, y, z\}$ in both the column and row index. In the $\tilde{\mathbf{Q}}$ tensor, Voigt notation was used instead for the column

index where the Cartesian directions $\{xx, yy, zz, yz, xz, xy\}$ were contracted to $\{1, 2, 3, 4, 5, 6\}$. The nonzero components of these tensors are tabulated in Table II. Due to the lack of values for 4H-SiC in the literature, we included experimental and theoretical values for 3C or 6H polytypes for comparison. Similar to that of 6H-SiC [68], the axial component ε_{33}^∞ is greater than the in-plane component ε_{11}^∞ in 4H-SiC. The Born effective charges of 4H-SiC are also close to the effective value for 6H-SiC determined from Raman spectra [69]. Additionally, it is apparent that while the in-plane component Z_{11} is only slightly different between h and k sites, the axial component Z_{33} is strongly site dependent. Such a difference should be associated with the geometry of h and k sites, which are different only in the stacking order along the c axis. Only 3C-SiC $\tilde{\mathbf{Q}}$ is available in the literature, and the symmetry is very different from 4H-SiC, so we cannot make direct comparison between $\tilde{\mathbf{Q}}$ tensors in 3C and 4H-SiC. However, we note that in general, the dynamical quadrupole charge for Si is significantly greater than that of C in both polytypes, suggesting a similar bond type and charge transfer between Si and C atoms.

[1] T. Kimoto and J. A. Cooper, *Fundamentals of Silicon Carbide Technology* (John Wiley & Sons Singapore, Singapore, 2014).

[2] J. Millan, P. Godignon, X. Perpina, A. Perez-Tomas, and J. Rebollo, A survey of wide bandgap power semiconductor devices, IEEE Trans. Power Electr. **29**, 2155 (2014).

[3] T. Kimoto, Material science and device physics in SiC technology for high-voltage power devices, Jpn. J. Appl. Phys. **54**, 040103 (2015).

[4] K. Puschkarsky, T. Grasser, T. Aichinger, W. Gustin, and H. Reisinger, Review on SiC MOSFETs high-voltage device

reliability focusing on threshold voltage instability, IEEE Trans. Electron Devices **66**, 4604 (2019).

[5] L. Han, L. Liang, Y. Kang, and Y. Qiu, A review of SiC IGBT: Models, fabrications, characteristics, and applications, IEEE Trans. Power Electron. **36**, 2080 (2021).

[6] R. Tian, C. Ma, J. Wu, Z. Guo, X. Yang, and Z. Fan, A review of manufacturing technologies for silicon carbide superjunction devices, J. Semicond. **42**, 061801 (2021).

[7] X. Liu, R. Wang, J. Zhang, Y. Lu, Y. Zhang, D. Yang, and X. Pi, Anisotropic deformation of 4H-SiC wafers: insights from nanoindentation tests, J. Phys. D **55**, 494001 (2022).

[8] Y. Huang, R. Wang, Y. Zhang, D. Yang, and X. Pi, Compensation of p-type doping in Al-doped 4H-SiC, J. Appl. Phys. **131**, 185703 (2022).

[9] H. Iwata and K. M. Itoh, Donor and acceptor concentration dependence of the electron Hall mobility and the hall scattering factor in n-type 4H- and 6H-SiC, J. Appl. Phys. **89**, 6228 (2001).

[10] A. Parisini and R. Nipoti, Analysis of the hole transport through valence band states in heavy Al doped 4H-SiC by ion implantation, J. Appl. Phys. **114**, 243703 (2013).

[11] S. Asada, T. Okuda, T. Kimoto, and J. Suda, Hall scattering factors in p-type 4H-SiC with various doping concentrations, Appl. Phys. Express **9**, 041301 (2016).

[12] H. Tanaka, S. Asada, T. Kimoto, and J. Suda, Theoretical analysis of Hall factor and hole mobility in p-type 4H-SiC considering anisotropic valence band structure, J. Appl. Phys. **123**, 245704 (2018).

[13] R. Ishikawa, M. Hara, H. Tanaka, M. Kaneko, and T. Kimoto, Electron mobility along $\langle 0001 \rangle$ and $\langle 1-100 \rangle$ directions in 4H-SiC over a wide range of donor concentration and temperature, Appl. Phys. Express **14**, 061005 (2021).

[14] J. Wozny, A. Kovalchuk, Z. Lisik, J. Podgorski, P. Bugalski, A. Kubiak, and Ł. Ruta, Monte Carlo simulations of electron transport in 4H-SiC using the DFT-calculated density of states, J. Comput. Electron. **20**, 791 (2021).

[15] F. Giustino, Electron-phonon interactions from first principles, Rev. Mod. Phys. **89**, 015003 (2017).

[16] S. Poncé, D. Jena, and F. Giustino, Route to High Hole Mobility in GaN via Reversal of Crystal-Field Splitting, Phys. Rev. Lett. **123**, 096602 (2019).

[17] S. Poncé and F. Giustino, Structural, electronic, elastic, power, and transport properties of β-Ga$_2$O$_3$ from first principles, Phys. Rev. Res. **2**, 033102 (2020).

[18] S. Poncé, F. Macheda, E. R. Margine, N. Marzari, N. Bonini, and F. Giustino, First-principles predictions of Hall and drift mobilities in semiconductors, Phys. Rev. Res. **3**, 043022 (2021).

[19] J. Ma, R. Yang, and H. Chen, A large modulation of electron-phonon coupling and an emergent superconducting dome in doped strong ferroelectrics, Nat. Commun. **12**, 2314 (2021).

[20] F. Giustino, J. R. Yates, I. Souza, M. L. Cohen, and S. G. Louie, Electron-Phonon Interaction via Electronic and Lattice Wannier Functions: Superconductivity in Boron-Doped Diamond Reexamined, Phys. Rev. Lett. **98**, 047005 (2007).

[21] C. Verdi, F. Caruso, and F. Giustino, Origin of the crossover from polarons to Fermi liquids in transition metal oxides, Nat. Commun. **8**, 15769 (2017).

[22] W. H. Sio, C. Verdi, S. Poncé, and F. Giustino, Polarons from First Principles, without Supercells, Phys. Rev. Lett. **122**, 246403 (2019).

[23] J. Noffsinger, E. Kioupakis, C. G. Van de Walle, S. G. Louie, and M. L. Cohen, Phonon-Assisted Optical Absorption in Silicon from First Principles, Phys. Rev. Lett. **108**, 167402 (2012).

[24] F. Giustino, S. G. Louie, and M. L. Cohen, Electron-Phonon Renormalization of the Direct Band Gap of Diamond, Phys. Rev. Lett. **105**, 265501 (2010).

[25] W. Li and F. Giustino, Many-body renormalization of the electron effective mass of InSe, Phys. Rev. B **101**, 035201 (2020).

[26] S. Poncé, W. Li, S. Reichardt, and F. Giustino, First-principles calculations of charge carrier mobility and conductivity in bulk semiconductors and two-dimensional materials, Rep. Prog. Phys. **83**, 036501 (2020).

[27] T. Deng, G. Wu, M. B. Sullivan, Z. M. Wong, K. Hippalgaonkar, J.-S. Wang, and S.-W. Yang, EPIC STAR: A reliable and efficient approach for phonon- and impurity-limited charge transport calculations, npj Comput. Mater. **6**, 46 (2020).

[28] G. Brunin, H. P. C. Miranda, M. Giantomassi, M. Royo, M. Stengel, M. J. Verstraete, X. Gonze, G. M. Rignanese, and G. Hautier, Electron-Phonon beyond Fröhlich: Dynamical Quadrupoles in Polar and Covalent Solids, Phys. Rev. Lett. **125**, 136601 (2020).

[29] G. Brunin, H. P. C. Miranda, M. Giantomassi, M. Royo, M. Stengel, M. J. Verstraete, X. Gonze, G. M. Rignanese, and G. Hautier, Phonon-limited electron mobility in Si, GaAs, and GaP with exact treatment of dynamical quadrupoles, Phys. Rev. B **102**, 094308 (2020).

[30] J. Park, J. J. Zhou, V. A. Jhalani, C. E. Dreyer, and M. Bernardi, Long-range quadrupole electron-phonon interaction from first principles, Phys. Rev. B **102**, 125203 (2020).

[31] V. A. Jhalani, J. J. Zhou, J. Park, C. E. Dreyer, and M. Bernardi, Piezoelectric Electron-Phonon Interaction from *Ab Initio* Dynamical Quadrupoles: Impact on Charge Transport in Wurtzite GaN, Phys. Rev. Lett. **125**, 136602 (2020).

[32] D. C. Desai, B. Zviazhynski, J.-J. Zhou, and M. Bernardi, Magnetotransport in semiconductors and two-dimensional materials from first principles, Phys. Rev. B **103**, L161103 (2021).

[33] F. Macheda and N. Bonini, Magnetotransport phenomena in p-doped diamond from first principles, Phys. Rev. B **98**, 201201(R) (2018).

[34] P. Giannozzi, S. Baroni, N. Bonini, M. Calandra, R. Car, C. Cavazzoni, D. Ceresoli, G. L. Chiarotti, M. Cococcioni, I. Dabo *et al.*, QUANTUM ESPRESSO: A modular and open-source software project for quantum simulations of materials, J. Phys.: Condens. Matter **21**, 395502 (2009).

[35] P. Giannozzi, O. Andreussi, T. Brumme, O. Bunau, M. B. Nardelli, M. Calandra, R. Car, C. Cavazzoni, D. Ceresoli, M. Cococcioni *et al.*, Advanced capabilities for materials modelling with QUANTUM ESPRESSO, J. Phys.: Condens. Matter **29**, 465901 (2017).

[36] F. Giustino, M. L. Cohen, and S. G. Louie, Electron-phonon interaction using Wannier functions, Phys. Rev. B **76**, 165108 (2007).

[37] N. Marzari, A. A. Mostofi, J. R. Yates, I. Souza, and D. Vanderbilt, Maximally localized Wannier functions: Theory and applications, Rev. Mod. Phys. **84**, 1419 (2012).

[38] G. Pizzi, V. Vitale, R. Arita, S. Blügel, F. Freimuth, G. Géranton, M. Gibertini, D. Gresch, C. Johnson, T. Koretsune *et al.*, Wannier90 as a community code: New features and applications, J. Phys.: Condens. Matter **32**, 165902 (2020).

[39] J. Noffsinger, F. Giustino, B. D. Malone, C.-H. Park, S. G. Louie, and M. L. Cohen, EPW: A program for calculating the electron-phonon coupling using maximally localized Wannier functions, Comput. Phys. Commun. **181**, 2140 (2010).

[40] S. Poncé, E. Margine, C. Verdi, and F. Giustino, Epw: Electronphonon coupling, transport and superconducting properties using maximally localized Wannier functions, Comput. Phys. Commun. **209**, 116 (2016).

[41] C. Verdi and F. Giustino, Fröhlich Electron-Phonon Vertex from First Principles, Phys. Rev. Lett. **115**, 176401 (2015).

[42] J. Sjakste, N. Vast, M. Calandra, and F. Mauri, Wannier interpolation of the electron-phonon matrix elements in polar semiconductors: Polar-optical coupling in GaAs, Phys. Rev. B **92**, 054307 (2015).

[43] J.-J. Zhou and M. Bernardi, *Ab initio* electron mobility and polar phonon scattering in GaAs, Phys. Rev. B **94**, 201201(R) (2016).

[44] S. Baroni, S. D. Gironcoli, A. D. Corso, and P. Giannozzi, Phonons and related crystal properties from density-functional perturbation theory, Rev. Mod. Phys. **73**, 515 (2001).

[45] M. Royo and M. Stengel, First-Principles Theory of Spatial Dispersion: Dynamical Quadrupoles and Flexoelectricity, Phys. Rev. X **9**, 021050 (2019).

[46] X. Gonze, B. Amadon, G. Antonius, F. Arnardi, L. Baguet, J.-M. Beuken, J. Bieder, F. Bottin, J. Bouchet, E. Bousquet *et al.*, The ABINIT project: Impact, environment and recent developments, Comput. Phys. Commun. **248**, 107042 (2020).

[47] A. H. Romero, D. C. Allan, B. Amadon, G. Antonius, T. Applencourt, L. Baguet, J. Bieder, F. Bottin, J. Bouchet, E. Bousquet *et al.*, ABINIT: Overview and focus on selected capabilities, J. Chem. Phys. **152**, 124102 (2020).

[48] J. P. Perdew, A. Ruzsinszky, G. I. Csonka, O. A. Vydrov, G. E. Scuseria, L. A. Constantin, X. Zhou, and K. Burke, Restoring the Density-Gradient Expansion for Exchange in Solids and Surfaces, Phys. Rev. Lett. **100**, 136406 (2008).

[49] M. van Setten, M. Giantomassi, E. Bousquet, M. Verstraete, D. Hamann, X. Gonze, and G.-M. Rignanese, The PSEUDODOJO: Training and grading a 85 element optimized norm-conserving pseudopotential table, Comput. Phys. Commun. **226**, 39 (2018).

[50] A. Marini, C. Hogan, M. Grüning, and D. Varsano, yambo: An *ab initio* tool for excited state calculations, Comput. Phys. Commun. **180**, 1392 (2009).

[51] D. Sangalli, A. Ferretti, H. Miranda, C. Attaccalite, I. Marri, E. Cannuccia, P. Melo, M. Marsili, F. Paleari, A. Marrazzo *et al.*, Many-body perturbation theory calculations using the yambo code, J. Phys.: Condens. Matter **31**, 325902 (2019).

[52] J. Heyd, G. E. Scuseria, and M. Ernzerhof, Hybrid functionals based on a screened Coulomb potential, J. Chem. Phys. **118**, 8207 (2003).

[53] J. Heyd, G. E. Scuseria, and M. Ernzerhof, Erratum: Hybrid functionals based on a screened coulomb potential [J. Chem. Phys. 118, 8207 (2003)], J. Chem. Phys. **124**, 219906 (2006).

[54] D. Volm, B. K. Meyer, D. M. Hofmann, W. M. Chen, N. T. Son, C. Persson, U. Lindefelt, O. Kordina, E. Sörman, A. O. Konstantinov *et al.*, Determination of the electron effective-mass tensor in 4*H* SiC, Phys. Rev. B **53**, 15409 (1996).

[55] N. T. Son, P. N. Hai, W. M. Chen, C. Hallin, B. Monemar, and E. Janzén, Hole effective masses in 4*H* SiC, Phys. Rev. B **61**, R10544 (2000).

[56] S. Poncé, E. R. Margine, and F. Giustino, Towards predictive many-body calculations of phonon-limited carrier mobilities in semiconductors, Phys. Rev. B **97**, 121201 (2018).

[57] M. Bauer, A. M. Gigler, A. J. Huber, R. Hillenbrand, and R. W. Stark, Temperature-depending Raman line-shift of silicon carbide, J. Raman Spectrosc. **40**, 1867 (2009).

[58] Yu.-I. Matsushita, S. Furuya, and A. Oshiyama, Floating Electron States in Covalent Semiconductors, Phys. Rev. Lett. **108**, 246404 (2012).

[59] Z. Li, P. Graziosi, and N. Neophytou, Deformation potential extraction and computationally efficient mobility calculations in silicon from first principles, Phys. Rev. B **104**, 195201 (2021).

[60] J. Pernot, S. Contreras, and J. Camassel, Electrical transport properties of aluminum-implanted 4H–SiC, J. Appl. Phys. **98**, 023706 (2005).

[61] G. Wagner, W. Leitenberger, K. Irmscher, F. Schmid, M. Laube, and G. Pensl, Aluminum incorporation into 4H-SiC layers during epitaxial growth in a hot-wall CVD system, Mater. Sci. Forum **389–393**, 207 (2002).

[62] S. Contreras, L. Konczewicz, R. Arvinte, H. Peyre, T. Chassagne, M. Zielinski, and S. Juillaguet, Electrical transport properties of p-type 4H-SiC, Phys. Status Solidi A **214**, 1600679 (2017).

[63] M. Lundstrom, *Fundamentals of Carrier Transport* (Cambridge University Press, Cambridge, 2000).

[64] T.-H. Liu, J. Zhou, B. Liao, D. J. Singh, and G. Chen, First-principles mode-by-mode analysis for electron-phonon scattering channels and mean free path spectra in GaAs, Phys. Rev. B **95**, 075206 (2017).

[65] F. Meng, J. Ma, J. He, and W. Li, Phonon-limited carrier mobility and temperature-dependent scattering mechanism of 3*C*-SiC from first principles, Phys. Rev. B **99**, 045201 (2019).

[66] M. D. Jong, W. Chen, H. Geerlings, M. Asta, and K. A. Persson, A database to enable discovery and design of piezoelectric materials, Sci. Data **2**, 150053 (2015).

[67] I. Petousis, D. Mrdjenovich, E. Ballouz, M. Liu, D. Winston, W. Chen, T. Graf, T. D. Schladt, K. A. Persson, and F. B. Prinz, Data descriptor: High-throughput screening of inorganic compounds for the discovery of novel dielectric and optical materials, Sci. Data **4**, 160134 (2017).

[68] L. Patrick and W. J. Choyke, Static dielectric constant of SiC, Phys. Rev. B **2**, 2255 (1970).

[69] J. Liu and Y. K. Vohra, Raman Modes of 6*H* Polytype of Silicon Carbide to Ultrahigh Pressures: A Comparison with Silicon and Diamond, Phys. Rev. Lett. **72**, 4105 (1994).